PAPER

Check for updates

Compositional flexibility in irreducible antifluorite electrolytes for next-generation battery anodes†

Victor Landgraf, [ID] Mengfu Tu, Zhu Cheng, Alexandros Vasileiadis, [ID] Marnix Wagemaker [ID] * and Theodosios Famprikis [ID] *

Solid-state batteries currently receive ample attention due to their potential to outperform lithium-ion batteries in terms of energy density when featuring next-generation anodes such as lithium metal or silicon. One key remaining challenge is identifying solid electrolytes that combine high ionic conductivity with stability in contact with the highly reducing potentials of next-generation anodes. Fully reduced electrolytes, based on irreducible anions, offer a promising solution by avoiding electrolyte decomposition altogether. In this study, we demonstrate the compositional flexibility of the disordered antifluorite framework accessible by mechanochemical synthesis and leverage it to discover irreducible electrolytes with high ionic conductivities. We show that the recently investigated $Li_9N_2Cl_3$ and Li_5NCl_2 phases are part of the same solid solution of Li-deficient antifluorite phases existing on the $LiCl-Li_3N$ tie line with a general chemical formula of $Li_{1+2x}Cl_{1-x}N_x$ ($0.33 < x < 0.5$). Using density functional theory calculations, we identify the origin of the 5-order-of-magnitude conductivity increase of the $Li_{1+2x}Cl_{1-x}N_x$ phases compared to the structurally related rock-salt LiCl phase. Finally, we demonstrate that S_{Cl}- and Br_{Cl}-substituted analogues of the $Li_{1+2x}Cl_{1-x}N_x$ phases may be synthesized, enabling significant conductivity improvements by a factor of 10, reaching 0.2 mS cm^{-1} for $Li_{2.31}S_{0.41}Br_{0.14}N_{0.45}$. This investigation demonstrates for the first time that irreducible antifluorite-like phases are compositionally highly modifiable; this finding lays the ground for discovery of new compositions of irreducible antifluorite-like phases with even further increased conductivities, which could help eliminate solid-electrolyte decomposition and decomposition-induced Li losses on the anode side in high-performance next-generation batteries.

Introduction

Solid-state batteries have the potential to supersede conventional Li-ion batteries in terms of energy density and safety.[1,2] Three main advantages of solid electrolytes are as follows. (1) The solid nature of solid electrolytes potentially enables bipolar stacking of individual cells, increasing the overall pack energy density. (2) Solid electrolytes are typically less flammable than liquid equivalents and thus safer. (3) Solid electrolytes are potentially better compatible with high-energy anodes such as silicon or metallic lithium.[1,2] An initial challenge has been to develop solid electrolytes with sufficiently high ionic conductivities to compete with liquid electrolytes. In recent years, multiple derivatives of the argyrodite and $Li_{10}GeP_2S_{12}$ solid electrolytes have been developed with Li-ion conductivities beyond 10 mS cm^{-1}, thus exceeding the conductivities of their liquid equivalents.[3–6] Nevertheless, the main issue with all

known highly conducting (>1 mS cm^{-1}) solid electrolytes is that they are generally not (electro-)chemically stable at the high potentials of typical Li-ion battery cathodes nor at low potentials of desirable high-capacity anodes such as silicon or lithium metal. The electrochemical instability of solid electrolytes with electrodes inevitably leads to electrolyte decomposition at the electrolyte–electrode interfaces.[1,7] Electrolyte decomposition at the electrode interfaces causes lithium loss, formation of resistive interphases and contact loss between solid-electrolyte- and electrode particles, which are all directly linked to battery degradation and failure.[8,9]

This study aims to design solid electrolytes that are highly conducting and thermodynamically stable against the low potentials of desirable high-capacity anodes such as lithium metal and silicon. Such electrolytes would eliminate (electro) chemical degradation on the anode side and thus eliminate complications associated with electrolyte degradation. With regards to thermodynamic stability at low potentials, fully reduced phases become immediately pertinent; *i.e.* phases in which the only cation present is Li and in which all anions are in their lowest permitted formal oxidation state and thus irreducible.[10,11] Commonly known examples of such irreducible

3562 | *J. Mater. Chem. A*, 2025, **13**, 3562–3574

This journal is © The Royal Society of Chemistry 2025

phases are the lithium binaries LiCl, LiBr, Li_2S, LiI, LiF, Li_3N and Li_3P. While these phases all feature thermodynamic stability at the low potentials (<0 V vs. Li^+/Li), they are fraught with low ionic conductivities (<10^{-6} mS cm^{-1}), except for Li_3N, which is reported to have a conductivity of 0.5 mS cm^{-1}.[10,12] New irreducible phases were recently discovered by exploring the tie lines between the above-listed binaries using mechanochemical synthesis. Examples include the $Li_{2+x}S_{1-x}P_x$ phases reported by Szczuka et al.[11] and the $Li_{2+x}S_{1-x}N_x$ phases reported by Landgraf et al.;[13] both systems reaching high conductivities of 0.2 mS cm^{-1}. Additionally, the Li_5NCl_2 (ref. 10) and $Li_9N_2Cl_3$ (ref. 14) phases existing on the Li_3N–LiCl tie line were recently investigated. Li et al. demonstrated excellent stability against Li-metal, stability in dry air and high critical-current density for dendrite formation of 10 mA cm^{-2} for the $Li_9N_2Cl_3$ phase.[14] Additionally, excellent performance of $Li_9N_2Cl_3$ in full cells was demonstrated where $Li_9N_2Cl_3$ is used as an anolyte to protect the $Li_{2.73}Ho_{1.09}Cl_6$ halide electrolyte against a Li metal anode.[14] These results are promising, however an essential drawback remains the low room-temperature conductivity of $Li_9N_2Cl_3$ which is reported to be 0.04 mS cm^{-1}.[14] Moreover, the mechanistic origin of the increased conductivity of $Li_9N_2Cl_3$ phases compared to the structurally related rocksalt LiCl phase has not been established.

The present study develops compositional design strategies to improve the conductivity of $Li_9N_2Cl_3$ through the following advances:

(1) Synthetically, we demonstrate that the antifluorite framework is compositionally flexible; Li-deficient and Li-excess antifluorite phases can be mechanochemically stabilized. We find that the previously reported Li_5NCl_2 and $Li_9N_2Cl_3$ phases (ref. 15 and 16) are both members of the same solid solution of Li-deficient antifluorite phases on the Li_3N–LiCl tie line with the general chemical formula of $Li_{1+2x}Cl_{1-x}N_x$ with $0.33 < x < 0.5$. Additionally, we show that $Li_{1+2x}Cl_{1-x}N_x$ phases are compositionally highly modifiable; we synthesize S_{Cl}- and Br_{Cl}-substituted analogues boosting the ionic conductivities of $Li_{1+2x}Cl_{1-x}N_x$ phases by an order of magnitude enabling conductivity enhancements up to 0.2 mS cm^{-1} for $Li_{2.31}S_{0.41}Br_{0.14}N_{0.45}$.

(2) Computationally, we explain how introducing nitrogen into the LiCl anionic-framework brings tetrahedral and octahedral lithium sites closer in energy so that vacant sites become energetically accessible for diffusion. Our analysis of diffusion bottlenecks resolving the effect of the local anion coordination shows that nitrogen widens diffusion bottlenecks further facilitating Li diffusion.

(3) Finally, we find through both experiments and computations that the oxidation limit of the irreducible antifluorite-like phases is compositionally tunable and generally higher compared to Li_3N which may be a critical advantage to stabilize next-generation anodes.

Results and discussion

Our starting point for this work is our previous work on fully reduced electrolytes, showing the conductivity of Li_2S could be highly improved by dissolving Li_3N into the antifluorite Li_2S

phase.[13] Dissolving Li_3N in Li_2S results in a series of phases where N and S share sites (Fig. S1†). A solid solution exists with the general chemical formula $Li_{2+x}S_{1-x}N_x$ ($0 < x < {\sim}0.5$), exhibiting an anion-disordered Li-rich antifluorite crystal structure (Fig. S1†) and showing much higher conductivity (>0.2 mS cm^{-1} for $x = 0.5$) than the Li_2S host phase (10^{-6} mS cm^{-1}).[13] This motivated our investigation of whether a similar solid solution may be found between Li_3N and LiCl (schematically illustrated in Fig. 1a), and examine their functional solid–electrolyte properties. To answer this question, Li_3N and LiCl were mixed in different ratios, followed by a high-energy mechanochemical treatment (ball milling).
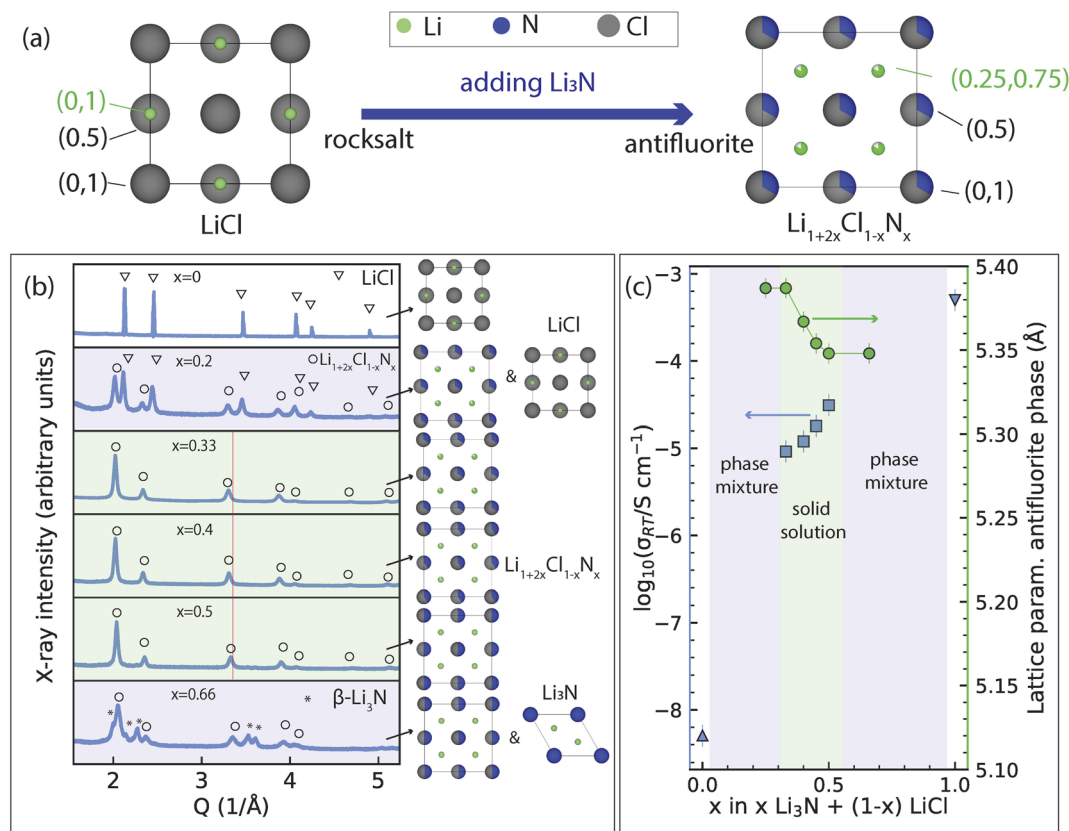
A solid solution of Li-deficient antifluorite phases on the Li_3N–LiCl tie line

Fig. 1 presents the results of the mechanochemical treatment of $xLi_3N + (1 - x)$LiCl samples and their resulting structure and ionic conductivities. Fig. 1a presents schematically the crystal structures of the parent LiCl rocksalt phase and the target antifluorite phases, confirmed by the powder X-ray diffraction experiments shown in Fig. 1b. Attempting to dissolve small quantities of Li_3N into LiCl did not result in a pure phase but a mixture of two cubic phases: LiCl and Li_5NCl_2. The stoichiometric formula of the latter may alternatively be written as $Li_{1.66}N_{0.33}Cl_{0.66}$ (i.e. $Li_{1+2x}Cl_{1-x}N_x$ with $x = 0.33$), and has been previously reported as a stable phase prepared by conventional solid-state synthesis.[10,15] Only when the $Li_{1.66}N_{0.33}Cl_{0.66}$ stoichiometry is reached, having a 2 : 1 LiCl/Li_3N ratio, a pure $Li_{1.66}N_{0.33}Cl_{0.66}$ phase is observed (i.e. the LiCl phase is not observed in the X-ray diffraction pattern). The mixtures with a higher nitrogen composition than the $Li_{1.66}N_{0.33}Cl_{0.66}$ phase ($Li_{1+2x}Cl_{1-x}N_x$ with $0.33 < x < 0.5$) show the same cubic $Fm\bar{3}m$ diffraction pattern as the $x = 0.33$ phase but with an increasing shift towards larger scattering vector Q indicating a decreasing lattice parameter with increasing nitrogen content. When exceeding an overall stoichiometry of $Li_2N_{0.5}Cl_{0.5}$ (i.e. $x = 0.5$) a second phase identified as β-Li_3N is observed in the diffraction pattern while the lattice parameter of the first phase remains constant. As expected based on the smaller ionic radius of N^{3-} compared to Cl^- (1.46 vs. 1.81 Å),[17] the lattice parameter of the $Li_{1+2x}Cl_{1-x}N_x$ phases decreases with increasing nitrogen content, where the linear shift is in accordance with Vegard's law (Fig. 1c). A solid-solution region of cubic $Li_{1+2x}Cl_{1-x}N_x$ phases is thus observed on the on the $xLiCl$–$(1 - x)Li_3N$ tie line for compositions between $0.33 < x < 0.5$, i.e. between the end members $Li_{1.66}N_{0.33}Cl_{0.66}$ and $Li_2N_{0.5}Cl_{0.5}$.

Rietveld refinements of the X-ray diffractograms (ESI Fig. S2 and Tables S1–4†) show that the crystal structure of the $Li_{1+2x}Cl_{1-x}N_x$ ($x < 0.33 < 0.5$) phases consist in a face-centered-cubic arrangement of the anions where N^{3-} and Cl^- share the same site. At the nitrogen-poor boundary of the solid solution (i.e. $Li_{1.66}N_{0.33}Cl_{0.66}$) the tetrahedral interstitials are partially occupied by Li ions (83%).‡ With increasing N content the Li content

---

‡ A small fraction of the Li ions ≤5% may potentially occupy the octahedral sites as detailed in ESI Note 1.

This journal is © The Royal Society of Chemistry 2025

J. Mater. Chem. A, 2025, **13**, 3562–3574 | **3563**

Fig. 1 Discovery of a new solid solution on the Li_3N–LiCl tie line. (a) View along the [001] of the unit cell of rock-salt LiCl and Li-deficient antifluorite $Li_{1+2x}Cl_{1-x}N_x$ phases (exact example of $x = 0.33$ shown). (b) X-ray diffraction pattern of the products of mechanochemically treating $xLi_3N + (1 − x)$LiCl mixtures. In the range ($x = 0.33$ to $x = 0.5$) phase-pure Li-deficient antifluorite structures are obtained. Phases existing at each overall composition are shown next to the diffraction patterns. Red line is guide to the eye. (c) Overall ionic conductivity at 22 °C determined experimentally *via* impedance spectroscopy and the lattice parameter of the antifluorite-like phase for different mixtures of $xLi_3N + (1 − x)$LiCl. Conductivity of (structurally distinct) Li_3N and LiCl are also shown for reference. Green and purple shading in (b) and (c) indicate solid-solution- and two-phase- regions, respectively.

increases to balance the charge, and the tetrahedral sites become increasingly populated until reaching the N-rich solid-solution boundary (*i.e.* $Li_2N_{0.5}Cl_{0.5}$). Consequently, where the $Li_2N_{0.5}Cl_{0.5}$ phase can be described as a (stoichiometric) antifluorite phase (with fully occupied tetrahedral sites), the solid-solution members with ($x < 0.5$) may be described as Li-deficient antifluorite phases (having only partially occupied tetrahedral sites). Further lithium insertion ($x > 0.5$) seems to destabilize the antifluorite, leading to decomposition into a mixture of $Li_2Cl_{0.5}N_{0.5}$ and Li_3N (Fig. 1b). This is in contrast to the lithium-rich antifluorites $Li_{2+x}S_{1-x}N_x$ which exhibit partial occupation of their octahedral sites in addition to full occupation of their tetrahedral sites (*vide infra*). The structural shift that occurs when going from rock-salt LiCl to Li-deficient antifluorite $Li_{1.66}N_{0.33}Cl_{0.66}$ entails a significant increase of the cubic lattice parameter from 5.17 Å to 5.39 Å (Fig. 1b), which is likely related to the rearrangement of lithium from the octahedral sites (in the former) to tetrahedral sites (in the latter).

Fig. 1c also shows the ambient-temperature ionic conductivity of the mechanochemically prepared samples as quantified by impedance spectroscopy experiments on pelletized samples which could be invariably fitted by a single bulk-diffusion

process (ESI Fig. S3†). The rock-salt LiCl phase has a conductivity of the order of 10^{-7} mS cm^{-1} (Fig. S4†). The conductivity of Li-deficient antifluorite $Li_{1.66}N_{0.33}Cl_{0.66}$ is significantly higher reaching 0.01 mS cm^{-1}, and introducing more nitrogen into the solid solution further increases the conductivity up to 0.03 mS cm^{-1} for $Li_2N_{0.5}Cl_{0.5}$ as shown in Fig. 1c.

We have thus discovered a new solid solution on the LiCl–Li_3N tie line with the general formula $Li_{1+2x}Cl_{1-x}N_x$ ($x < 0.33 < 0.5$) accessible by mechanochemistry (in contrast to conventional solid state synthesis previously explored in ref. 10 and 15). These phases crystallize in an anion disordered Li-deficient antifluorite-like crystal structure and their conductivity is orders of magnitude higher than the conductivity of rock-salt LiCl. In the next section, we will analyze the mechanistic origin of this 5-order-of-magnitude boost in ionic conductivity.

Rock-salt LiCl *vs.* Li-deficient antifluorite $Li_{1+2x}Cl_{1-x}N_x$ – origin of the improved conductivity

Fast Li diffusion relies on two prerequisites: (1) Li sites connected by low Li-hop activation energies into a percolating network and (2) a sufficient fraction of vacancies among these Li

3564 | *J. Mater. Chem. A*, 2025, **13**, 3562–3574

This journal is © The Royal Society of Chemistry 2025

sites. Vacant Li-sites may be introduced by defects (*e.g.* Frenkel defect pairs) and/or may be synthetically introduced *via* compositional tuning. To investigate Li diffusion in (defect-free) rock-salt LiCl and Li-deficient antifluorite $Li_{1+2x}Cl_{1-x}N_x$ phases we performed *ab initio* molecular dynamics (AIMD) simulations of $2 \times 2 \times 2$ supercells. As done in previous studies, we dissected our AIMD simulations into individual jump events.[10,18–21] From the frequency of jumps between two sites A and B ($\nu_{A \to B}$), we calculate jump-activation energies (jump-E_a) by using eqn (1) and assuming a prefactor frequency (ν_0) of 10^{13} Hz: §

$$\text{jump } E_{a, A \to B} = -k_b T \ln\left(\frac{\nu_{A \to B}}{\nu_0}\right) \quad (1)$$

where k_b is the Boltzmann constant, T the temperature in K, $\nu_{A \to B}$ the observed frequency of jumps between sites A and B and jump-$E_{a, A \to B}$ the jump-activation energy of a jump event from site A to site B. Details on this methodology may be found in ref. 18 and 22. We use these jump-activation energies as a proxy for the local energy barriers. From the difference between the activation energies of the forward and backward jump, the energy difference between two crystallographic positions may be approximated as follows (and illustrated in Fig. S5†):

$$\Delta E_{\text{site}}(A, B) = \text{jump-}E_{a, A \to B} - \text{jump-}E_{a, B \to A} \quad (2)$$

$\Delta E_{\text{site}}(\text{tet, oct})$ may be approximated from eqn (2) as the average of $\Delta E_{\text{site}}(A, B)$ for all sites where A and B are tetrahedral and octahedral sites respectively.

Fig. 2 presents the result of our analysis of molecular dynamics of rock-salt LiCl and Li-deficient antifluorite $Li_{1+2x}Cl_{1-x}N_x$ phases.

In LiCl, the octahedral interstitials are preferably occupied over the tetrahedral ones (Fig. 2a), indicating that the former are more stable than the latter. All tetrahedral interstitials in LiCl are vacant thus, in principle, LiCl features a high concentration of vacant interstitials enabling potential diffusion pathways *via* an octahedral–tetrahedral–octahedral jump sequence. $|\Delta E_{\text{site}}(\text{tet, oct})|$ is 0.61 ± 0.02 eV in the case of LiCl indicating that tetrahedral sites are on average significantly destabilized by *ca.* 0.6 eV *versus* octahedral sites. The jump-activation energy for the tet–oct jumps in LiCl is low (*ca.* 0.03 eV) suggesting that the tetrahedral site is highly metastable and should arguably more generally be referred to as 'position' than 'site' as further detailed in ESI Note 2.† For the remaining discussion of this work however this distinction will not be made and the tetrahedral positions in LiCl will also be referred to as sites. One potential reason for the high metastability of tetrahedral Li sites may be the small void space at the tetrahedral site enabling occupation of an ion with a max radius of 0.38 Å (see ESI Note 3†) which is smaller than the Li-ion radius

(0.59 Å).[17] Additionally, oct–tet transitions are sterically hindered in LiCl due to a highly constrained bottleneck with a diameter of 0.8 Å, which requires energetically unfavorably close Li–Cl ion distances and/or lattice distortion to accommodate the passing of Li ions (Fig. 2e). To summarize, in rock-salt LiCl, Li is confined to the octahedral sites and low-activation-energy jumps to vacant sites are not available, rationalizing the absence of diffusion during simulations (localized density in Fig. 2g) and the low RT ion conductivity of LiCl.¶

We now turn our attention to Li-diffusion in the $Li_{1.66}N_{0.33}Cl_{0.66}$ phase. We performed AIMD simulations on seven different disordered $Li_{1+2x}Cl_{1-x}N_x$ ($2 \times 2 \times 2$) supercells (including $Li_{1.66}N_{0.33}Cl_{0.66}$) to investigate the ion jumps and their jump activation energies present in these phases. Shared site occupations and partial occupancies in $Li_{1+2x}Cl_{1-x}N_x$ phases were treated by random decoration of the Wyckoff 4a (0, 0, 0) position with nitrogen and chlorine and the 8c (0.25, 0.25, 0.25). Li-positions were randomly decorated with Li and vacancies in order to reach the targeted stoichiometry (see Methodology for full computational details). In contrast to LiCl, in the Li-deficient antifluorite $Li_{1.66}N_{0.33}Cl_{0.66}$ structure the tetrahedral Li sites are occupied, indicating that they are stabilized with respect to the octahedral sites. $Li_{1.66}N_{0.33}Cl_{0.66}$ features two types of intrinsic vacancies. (1) The tetrahedral sites are partially occupied and (2) the octahedral interstitials are essentially vacant (Fig. 2b).‖ Compared to LiCl the difference in site energy between octahedral and tetrahedral is much smaller, with $|\Delta E_{\text{site}}(\text{tet–oct})| = 0.07 \pm 0.01$ eV as compared to $|\Delta E_{\text{site}}(\text{tet–oct})| = 0.61 \pm 0.02$ eV in LiCl (Fig. 2c and d). This flat(ter) energy landscape enables low-activation-energy oct–tet jumps and increased bulk diffusion reflected in the much more diffuse Li-density compared to the LiCl case (Fig. 2h) and higher experimentally-measured conductivities of $Li_{1.66}N_{0.33}Cl_{0.66}$ (Fig. 1c).

Fig. 3 presents our analysis of ion hopping in disordered $Li_{1+2x}Cl_{1-x}N_x$ as a function of local environment and jump geometry.

From our AIMD simulations we observe that diffusion occurs *via* Li jumps between oct and tet sites through triangular bottlenecks consisting of three anions as well as between tet sites through linear bottlenecks consisting of two anions (Fig. 3a). Li diffusion through triangular and linear bottlenecks is facilitated by the presence of N in the anionic lattice. Because N^{3-} (1.46 Å) anions are considerably smaller than Cl^- (1.81 Å) anions, the bottleneck becomes larger, enabling Li diffusion. To quantify this further, we calculated the bottleneck diameters for 5 $Li_{1.66}N_{0.33}Cl_{0.66}$ DFT relaxed ($2 \times 2 \times 2$) supercells (featuring >500 bottlenecks) to account for local distortions that may not

---

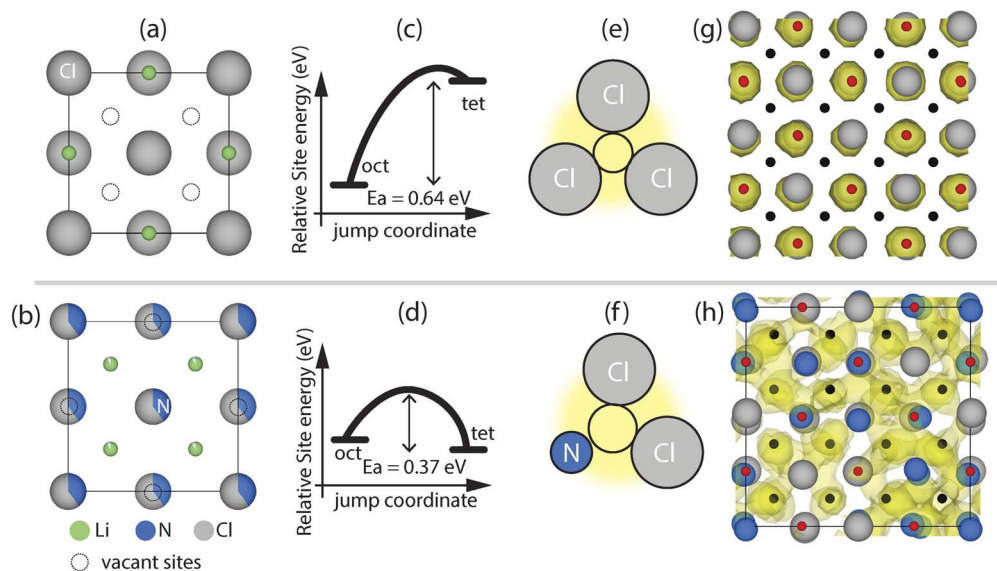§ Assuming $\nu_0 = 10^{13}$ s^{-1} is commonly adopted in the solid electrolyte field.[19,43,44] Additionally we justify this choice by calculating the average vibration frequency around the equilibrium Li-sites in our AIMD simulations and find it to be 1.0 ± 0.2 10^{13} Hz for 5 different $Li_{1+2x}Cl_{1-x}N_x$ supercells (Table S5).

¶ Due to the high activation energy required for oct–tet jumps in LiCl and the high metastability of tet sites/positions diffusion in LiCl is likely mediated by Schottky defects just as in NaCl. Accordingly, the charge carrier concentration in LiCl at room temperature is extremely low ($\sim 1 \times 10^{-9}$ c_{Li} where c_{Li} is the Li concentration in LiCl) as the formation energy for Schottky defects is typically ~ 1 eV. This low charge carrier concentration additionally contributes to the low ionic conductivity in LiCl.

‖ Potentially a small fraction of Li ions ≤5% on average may occupy the octahedral sites in which case the octahedral sites as detailed in ESI Note 1.

This journal is © The Royal Society of Chemistry 2025

J. Mater. Chem. A, 2025, **13**, 3562–3574 | **3565**

Fig. 2 Comparison lithium diffusion in LiCl and $Li_{1+2x}Cl_{1-x}N_x$ phases *via ab initio* molecular dynamics simulations. (a) and (b) View along the [001] of the unit cell of rock-salt LiCl and Li-deficient antifluorite $Li_{1+2x}Cl_{1-x}N_x$ phases. (c) and (d) Schematic illustration of the energy difference and average jump-activation energy between tetrahedral and octahedral sites in rock-salt LiCl and Li-deficient antifluorite $Li_{1+2x}Cl_{1-x}N_x$ phases. (e) and (f) Schematics of the triangular bottlenecks for oct–tet jumps. (g) and (h) LiCl and $Li_{1.8}Cl_{0.6}N_{0.4}$ supercell with the Li density of a 100 ps AIMD simulation at 1000 K. The Li density cutoff is set to 3% of the maximum value.

be evident in the average crystallographic unit cell. The bottleneck diameters for different bottlenecks as well as the average jump-E_a for jumps through the respective bottlenecks are shown in Fig. 3. Comparing the bottleneck diameter to the diameter of Li-ions (1.18 Å) is a good proxy for the constraints on Li diffusion; bottlenecks with significantly smaller diameters than 1.18 Å will constrain Li diffusion more than bottlenecks with diameters >1.18 Å. Fig. 3b for instance shows that triangular bottlenecks consisting of three chlorides are considerably smaller (∼0.8 Å) than bottlenecks containing one or more nitrogen (>1.25 Å). Fig. 3b and c show that jumps through nitrogen-containing bottlenecks for oct–tet and tet–tet jumps have lower activation energies indicating easier diffusion through N containing bottlenecks. Consequently, increasing the nitrogen content in the $Li_{1+2x}Cl_{1-x}N_x$ phase, results in more nitrogen-rich, low-activation-energy bottlenecks, explaining the increase in conductivity upon increasing the nitrogen content in the $Li_{1+2x}Cl_{1-x}N_x$ solid solution shown in Fig. 1c.

In conclusion, it is not possible to continuously dissolve Li_3N into rock-salt LiCl to form Li-excess rock-salt phases as the excess Li ions would occupy tetrahedral sites which are sterically too constrained to accommodate Li ions. However, once a critical amount of Li_3N ($x \geq 0.33$) is mixed with LiCl sufficient Li ions are available to stabilize (Li-deficient) antifluorite phases where Li ions occupy tetrahedral sites. The occupation of tetrahedral sites indicates that the tetrahedral sites are more stable than octahedral sites in Li-deficient antifluorite phases. The vacant octahedral sites and the occupied tetrahedral sites are energetically in close proximity ($|\Delta E_{site}(tet–oct)| \sim 0.07$ eV) and oct–tet (and tet–tet) transitions are facilitated by the presence of N^{3-} anions in the anionic lattice as the smaller ionic radius of N^{3-} compared to Cl^- increases the bottleneck size (Fig. 2f and 3). Consequently, the

vacant octahedral sites which are innate to Li-deficient antifluorite phases are thermodynamically and kinetically accessible so that tet–oct jumps may be achieved with jump-E_a values of 0.37 ± 0.01 eV on average. In contrast, in LiCl the vacant tetrahedral sites are at much larger energies than the occupied octahedral sites ($|\Delta E_{site}(tet–oct)| \sim 0.6$ eV). Additionally, the oct–tet transitions are sterically hindered by small bottlenecks consisting of 3 Cl^- ions so that an oct–tet transition has a jump-E_a value of 0.64 ± 0.01 eV on average. Consequently, the vacant tetrahedral sites which are innate to rock-salt LiCl phases are thermodynamically and kinetically inaccessible explaining the absence of diffusion in simulations and the experimentally obtained low ionic conductivity.

Comparison between Li-rich antifluorite $Li_{2+x}S_{1-x}N_x$ and Li-deficient antifluorite $Li_{1+2x}Cl_{1-x}N_x$

The presently discovered $Li_{1+2x}Cl_{1-x}N_x$ ($0.33 < x < 0.5$) solid-solution phases are a structural analog of the $Li_{2+x}S_{1-x}N_x$ ($0 < x < \sim0.5$) system previously discovered.[13] Comparing the $Li_{1+2x}Cl_{1-x}N_x$ and $Li_{2+x}S_{1-x}N_x$ phases in the ($0.33 < x < 0.5$) range, where both exist as solid solutions, is insightful in understanding the relationship between structure and Li-ion conductivity. For this we consider three phases of each solid solution, $x = 0.33$, $x = 0.4$ and $x = 0.45$, —representing the lower, center and upper limit of the $0.33 < x < 0.5$ range, respectively—and compare their ionic conductivity metrics as quantified by variable-temperature impedance spectroscopy. Fig. 4 presents the resulting dependence of the ambient-temperature conductivity, activation energy and conductivity prefactor as a function of composition in $Li_{1+2x}Cl_{1-x}N_x$ and $Li_{2+x}S_{1-x}N_x$.

3566 | *J. Mater. Chem. A*, 2025, 13, 3562–3574

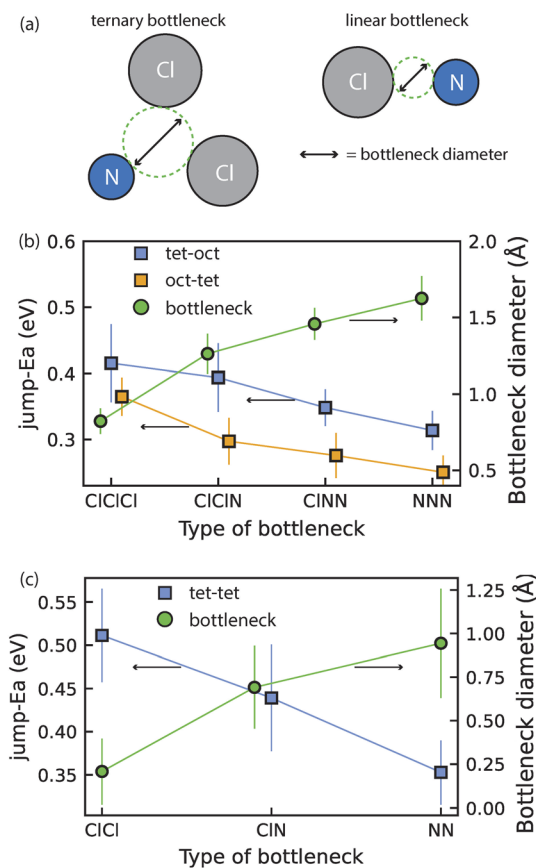This journal is © The Royal Society of Chemistry 2025

Fig. 3 Jump activation energies and bottleneck sizes for ion hops through specific bottlenecks. (a) Schematic of triangular and linear bottlenecks connecting oct–tet and tet–tet site pairs, respectively. (b) Average activation energy of tet–oct and oct–tet jumps for different bottleneck compositions along with the bottleneck size. Error bars are the standard deviation of the distribution of observed bottleneck sizes and activation energies. (c) Same as (b) for tet–tet jumps.

A notable difference is that the $Li_{2+x}S_{1-x}N_x$ phases are Li-excess antifluorite structures (more than 2 Li per anion), with partial Li occupancy of the octahedral sites (ref. 13) while the $Li_{1+2x}Cl_{1-x}N_x$ phases are Li-deficient antifluorite phases (less than 2 Li per anion) where the tetrahedral sites are partially occupied by Li (Fig. S1 and 2†). Fig. 4a shows that the Li-excess $Li_{2+x}S_{1-x}N_x$ phases have much higher ($\sim 10\times$) conductivity than the Li-deficient $Li_{1+2x}Cl_{1-x}N_x$ phases, whereas the bulk activation energies, determined by EIS, for the $Li_{2+x}S_{1-x}N_x$ and the $Li_{1+2x}Cl_{1-x}N_x$ phases differ by at most 0.03 eV (Fig. 4b) suggesting that the energy thresholds for diffusion in both systems are similar. However, the difference in the Arrhenius perfactors is large, on average a factor of 7 larger for the phases compared to of the $Li_{1+2x}Cl_{1-x}N_x$ phases (Fig. 4c). This suggests that the origin of the higher conductivity of $Li_{2+x}S_{1-x}N_x$ phases is largely comprised in the Arrhenius prefactor. The larger charge carrier concentration in $Li_{2+x}S_{1-x}N_x$ (and potentially the inducing of concerted motion though we do not explicitly investigate this here) are likely the origin for the larger Arrhenius prefactor of Li-excess $Li_{2+x}S_{1-x}N_x$ antifluorite phases.
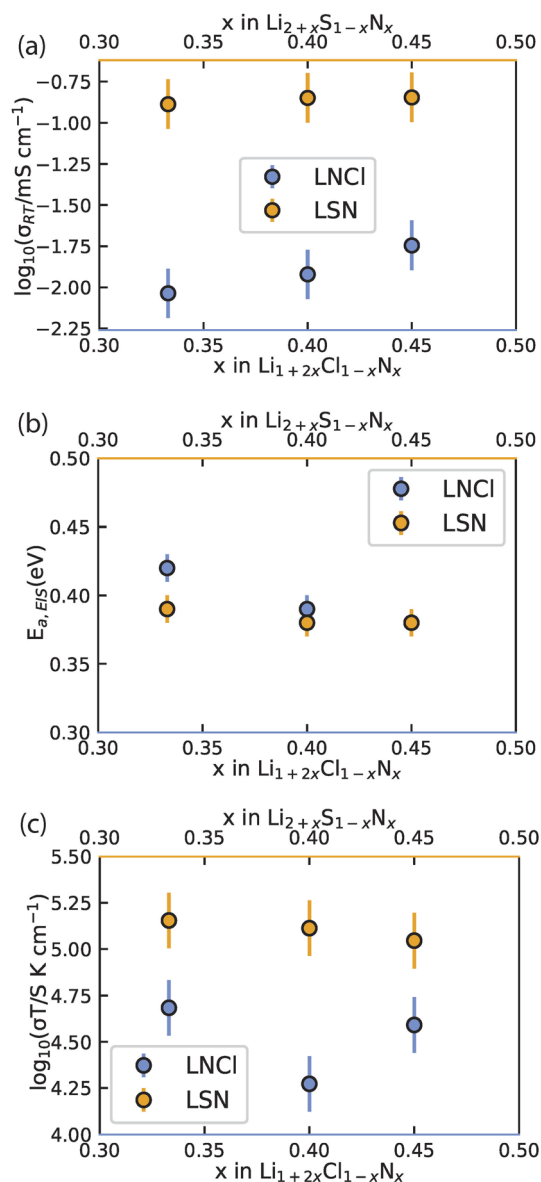

Fig. 4 Comparison of the experimentally obtained conductivity, activation energy and Arrhenius prefactor of $Li_{1+2x}Cl_{1-x}N_x$ and $Li_{2+x}S_{1-x}N_x$ phases. (a) Comparison of the conductivity at 22 °C determined experimentally via impedance spectroscopy. (b) Comparison of the Arrhenius plot for the activation energy. (c) Comparison of the Arrhenius prefactor. Data for $Li_{2+x}S_{1-x}N_x$ originally reported in ref. 13. The Arrhenius fits for (b) are shown in Fig. S6.†

Oxidation limits of Li-rich antifluorite $Li_{2+x}S_{1-x}N_x$ and Li-deficient antifluorite $Li_{1+2x}Cl_{1-x}N_x$ phases

We computationally investigated the metastability of $Li_{2+x}S_{1-x}N_x$ and $Li_{1+2x}Cl_{1-x}N_x$ antifluorite-like phases. For compositions $x = 0.11, 0.17, 0.36, 0.55, 0.72$ we built 10 000 random $2 \times 2 \times 2$ antifluorite-like $Li_{2+x}S_{1-x}N_x$ supercells and calculated their electrostatic energies with the formal oxidation states Li^+, S^{2-} and N^{3-} assigned to the ions. We took the 30 supercells with the lowest electrostatic energies and relaxed the structures using density functional theory. With the energies obtained, the energy above the hull of these phases was calculated using

This journal is © The Royal Society of Chemistry 2025

J. Mater. Chem. A, 2025, 13, 3562–3574 | 3567

entries of the materials project database (see also ESI Note 4†). Fig. 5 compares the calculated energies with the experimentally obtained stability limits of $Li_{2+x}S_{1-x}N_x$ and $Li_{1+2x}Cl_{1-x}N_x$ as a function of composition.

Fig. 5a shows the average energy above the hull for the $Li_{2+x}S_{1-x}N_x$ phases and shows that increased nitrogen content and Li stuffing increase metastability (*i.e.* higher energy above the hull). Note the energy above the hull was calculated for antifluorite-like $Li_{2+x}S_{1-x}N_x$ phases even at nitrogen contents that cannot be stabilized experimentally (*i.e.* $x > 0.55$) to clearly demonstrate the effect of Li_3N dissolution into Li_2S on phase (meta)stability.

Turning to the $Li_{1+2x}Cl_{1-x}N_x$ phases, the metastability of $Li_{1+2x}Cl_{1-x}N_x$ phases was calculated in an analogous manner to the $Li_{2+x}S_{1-x}N_x$ phases and is shown in Fig. 5b. Note the energy above the hull is calculated for antifluorite-like $Li_{1+2x}Cl_{1-x}N_x$ phases even at nitrogen contents that cannot be stabilized

experimentally (*i.e.* $x < 0.33$ and $x > 0.5$) to clearly demonstrate the effect of nitrogen content on phase (meta)stability. For $Li_{1+2x}Cl_{1-x}N_x$ phases the metastability is high at low and at high nitrogen content. The metastability of $Li_{1+2x}Cl_{1-x}N_x$ phases is lowest around the center of the $LiCl–Li_3N$ tie line. This non-monotonic trend in the metastability is consistent with the experimentally observed low-N-content and high-N-content boundaries of the $Li_{1+2x}Cl_{1-x}N_x$ ($0.33 < x < 0.5$) solid solution (Fig. 1b and c).

Fig. 5c presents the oxidative stability limits of the $Li_{2+x}S_{1-x}N_x$ and $Li_{1+2x}Cl_{1-x}N_x$ antifluorite-like phases as determined experimentally by linear-sweep voltammetry (ESI Fig. S7 and S8†). The trends in the experimental oxidative limits mirror the trends observed for energy above the hull in Fig. 5a and b: the increased metastability of N-rich antifluorite-like $Li_{2+x}S_{1-x}N_x$ phases is reflected in the oxidation stability which mono-tonically decreases the higher the nitrogen content and a non-monotonic trend is observed in the oxidation stability of $Li_{1+2x}Cl_{1-x}N_x$ phases with a maximum for $x = 0.4$.

S_{Cl} and Br_{Cl} substitutions on $Li_{1+2x}Cl_{1-x}N_x$ phases to boost conductivity

In this section we investigate the effect of S_{Cl} and Br_{Cl} substitutions in $Li_{1+2x}Cl_{1-x}N_x$ phases. S_{Cl} substitutions in $Li_{1+2x}Cl_{1-x}N_x$ may increase the number of charge carriers and Br_{Cl} substitutions could increase the lattice parameter facilitating Li diffusion. To narrow down this vast compositional space, the effect of the S_{Cl}, Br_S and Br_{Cl} substitutions considered at a fixed nitrogen content $x = 0.45$. Thus the phase space we set out to investigate can be expressed by the following solid-solution formula: $Li_{1.9+0.55y}Cl_{0.55(1-y-z)}S_{0.55y}Br_{0.55z}N_{0.45}$ ($0 < y,z < 1$). We explored the ionic conductivity of this phase space by synthesizing various compositions in the ternary phase diagram and measuring their ionic conductivity using impedance spectroscopy (provided a single antifluorite-like phase was obtained). The results of this investigation are shown in ESI Fig. S9–S14.† Fig. 6 presents the ionic conductivity of ternary and quaternary $Li_{1.9+0.55y}Cl_{0.55(1-y-z)}S_{0.55y}Br_{0.55z}N_{0.45}$ antifluorite-like samples synthesized as a function of composition in a quasi-ternary phase diagram.

We find that nearly all compositions in the phase space shown in Fig. 6 exist as Li-deficient or Li-excess antifluorite structures. Only highly Br-rich samples where the bromine content exceeds 40% of all anions (that is, values of $z > 0.75$ in $Li_{1.9+0.55y}Cl_{0.55(1-y-z)}S_{0.55y}Br_{0.55z}N_{0.45}$) did not result in phase-pure antifluorite-like phases.

Three main trends may be derived from Fig. 6. (1) S_{Cl} substitutions entail a continuous increase in ionic conductivity. For instance, when substituting Cl in $Li_{1.9}Cl_{0.55}N_{0.45}$ by S to form $Li_{2.45}S_{0.55}N_{0.45}$ the conductivity increases by an order of magnitude (from 0.02 to 0.15 mS cm^{-1}). This trend can be rationalized based on the increased mobile charge-carrier concentration through charge compensation in replacing S^{2-} by Cl^- ions. (2) The second main trend we derive from Fig. 6 is that Br_{Cl} substitutions entail a continuous increase in ionic conductivity. For instance, substituting all Cl in
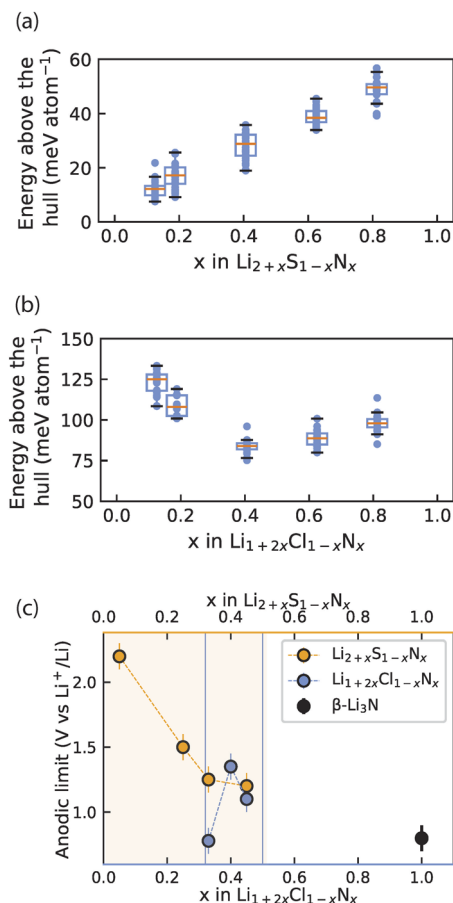

Fig. 5 Interplay of phase (meta)stability and anodic limit of irreducible antifluorite phases. (a) and (b) Calculated energy above the hull for 30 $Li_{2+x}N_xS_{1-x}$ and $Li_{1+2x}Cl_{1-x}N_x$ antifluorite supercells at each of several compositions x. At each composition above the distribution of energies above the hull is shown as a box plot where the orange line indicates the arithmetic mean and the box indicates the first standard deviation. (c) Experimental anodic limits obtained from LSV for $Li_{2+x}S_{1-x}N_x$, $Li_{1+2x}Cl_{1-x}N_x$ and β-Li_3N for reference. Orange shading and blue lines denote the solid–solution range for $Li_{2+x}S_{1-x}N_x$ and $Li_{1+2x}Cl_{1-x}N_x$ respectively. Data for $Li_{2+x}S_{1-x}N_x$ in (c) originally reported in ref. 13.

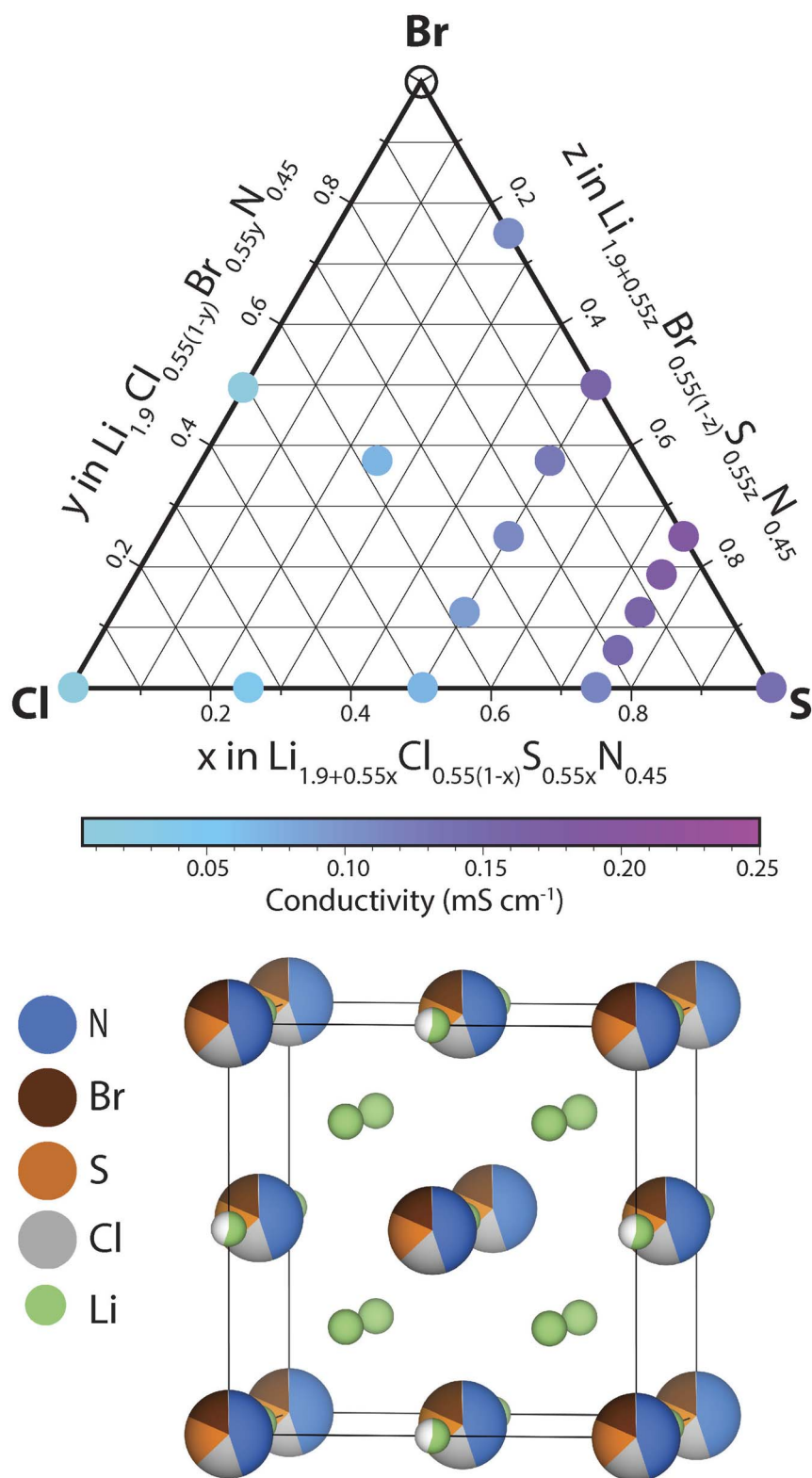**3568** | *J. Mater. Chem. A*, 2025, **13**, 3562–3574

This journal is © The Royal Society of Chemistry 2025

Fig. 6 Investigating conductivities in the $Li_{1.9+0.55y}Cl_{0.55(1-y-z)}S_{0.55y}Br_{0.55z}N_{0.45}$ ($0 < y, z < 1$) space. Quasi-ternary phase diagram with the $Li_{1.9}Cl_{0.55}N_{0.45}$, $Li_{1.9}Br_{0.55}N_{0.45}$ and the $Li_{2.45}S_{0.55}N_{0.45}$ compositions at its vertices. The circles represent the phase-compositions that were synthesized as part of this work. Coloured circles signify pure-phase antifluorite-like products. Hollow circles signify no pure-phase antifluorite-like phase product. The colors correspond to experimentally measured ionic conductivities at 22 °C. A schematic unit cell of the phase space investigated is also shown.

This journal is © The Royal Society of Chemistry 2025

J. Mater. Chem. A, 2025, 13, 3562–3574 | 3569

$Li_{2.175}Cl_{0.275}S_{0.275}N_{0.45}$ by Br to form $Li_{2.175}Br_{0.275}S_{0.275}N_{0.45}$ leads to a conductivity increase by a factor of *ca.* 2. This trend may be rationalized by the larger ion radius of Br^- compared to Cl^-: the presence of Br^- increases the lattice parameter, which facilitates diffusion through the sterically constrained diffusion bottlenecks. Additionally, the higher polarizability (softness) of Br compared to Cl (ref. 23) may ease diffusion through Br-containing bottlenecks compared to Cl-containing bottlenecks. (3) The third trend we derive from Fig. 6 is that partial Br_S substitutions increase ionic conductivities. Unlike the two previous trends, this trend is not monotonic. While partial Br_S substitution leads to higher conductivities, carrying the substitution too far leads to decreasing conductivities. This discontinuous trend may be explained as follows. While Br_S substitutions increase the lattice parameter, Br_S substitutions concurrently reduce the Li concentration to compensate for the lower valence of Br^- compared to S^{2-} ions.

In agreement with the trends described above we find that the phase with the highest conductivity is a moderately Br-substituted $Li_{2.45}S_{0.55}N_{0.45}$ phase – that is a phase with a stoichiometry of $Li_{2.31}S_{0.41}Br_{0.14}N_{0.45}$ reaching a conductivity of *ca.* 0.2 mS cm^{-1} at 22 °C. Overall this investigation demonstrates the high structural and compositional flexibility of the antifluorite framework; Li-deficient and Li-rich antifluorite phases may be stabilized and may feature numerous elements on the anion site.

Perspectives of irreducible antifluorite-like electrolytes for batteries

Solid-state batteries necessitate high-energy, low-voltage anodes such as Li metal or Li_xSi to supersede conventional Li-ion batteries.[8,24] However, the best ion conductors known to date—reaching >0.1 mScm^{-1} in conductivity and comprising oxide, sulfide and halide chemistries suffer from electrochemical decomposition <1 V *vs.* Li/Li$^+$[7,25–27]—with the exception of garnet oxides which are compatible with Li metal.[28**] Electrochemical decomposition on the anode side is associated with increased cell resistance, capacity loss, dendrite formation and short-circuiting.[29,30] A promising strategy to avoid reductive decomposition are bilayer separators comprising a catholyte facing the cathode and an anolyte facing the anode.[1] Anolytes should be highly-conducting and electrochemically stable at the low potentials of Li metal anodes. Highly conducting fully-reduced phases are thus inherently promising anolyte candidates which has also been demonstrated experimentally.[13,14,31]

High conductivity and reductive stability are not the only criteria suitability criteria of anolytes. The suitability of anolyte layers is system-dependent and multiple factors need to be considered. Mechanical and microstructural properties of solid electrolytes play a key role, for instance in dendrite formation and mechanical degradation in solid-state batteries.[32,33] Chemical compatibilities of anolytes with the paired catholytes also need to be considered.[10] Additionally, the oxidation limit of

anolytes needs to be considered; for applications *e.g.* with Li_xSi anodes whose operation window ranges from 0.01 V to 1.1 V.[8] Due to the low oxidation limit of Li_3N (0.8 V *vs.* Li/Li$^+$), Li_3N would be inert to reduction but not inert to oxidation when in contact with Li_xSi anodes. In contrast, some compositions of the antifluorite-like phases have oxidation limits exceeding 1.1 V (see Fig. 5c) and would be suitable anolytes for Li_xSi anodes as they would be inert to reduction and oxidation. In summary, irreducible electrolytes are promising anolyte candidates. The high compositional and structural flexibility of fully-reduced antifluorite-like phases we demonstrate in this study will enable the further tunability of ionic conductivity, electrochemical stability, mechanical and microstructural properties – essential for functional electrode/electrolyte interfaces in batteries.[32]

Conclusion

Fully reduced electrolytes based on the antifluorite framework recently received ample attention as their stability against low potentials eliminates performance degradation due to reductive decomposition.[14] In this study we elucidated the mechanism underlying the increased conductivity in herein discovered irreducible antifluorite-like $Li_{1+2x}Cl_{1-x}N_x$ phases (which includes $Li_9N_2Cl_3$ ref. 14 and Li_5NCl_2 ref. 10 and 15) compared to the structurally similar LiCl phase. Computationally, we find that introducing nitrogen into the LiCl anionic framework brings tetrahedral and octahedral Li sites closer in energy so that vacant sites become energetically accessible for diffusion. Analyzing local diffusion bottlenecks we further showed that nitrogen widens diffusion bottlenecks further facilitating Li diffusion. Experimentally we demonstrated that the antifluorite framework is stoichiometrically flexible; Li-deficient and Li-excess antifluorite phases can be stabilized. We further found that fully reduced antifluorite-like phases have an increased oxidation limit compared to Li_3N (0.8 V *vs.* Li) which may be critical advantage over Li_3N (the archetypical fully reduced electrolyte) to stabilize next-generation anodes. Additionally, we showed that $Li_{1+2x}Cl_{1-x}N_x$ phases are compositionally highly modifiable: S_{Cl^-} and Br_{Cl^-}-substituted analogues were synthesized, boosting the ionic conductivities of $Li_{1+2x}Cl_{1-x}N_x$ phases by an order of magnitude. We demonstrate that ternary and quaternary solid solutions can be synthesized mechanochemically in the LiCl–LiBr–Li$_2$S–Li$_3$N phase space, unlocking an expansive compositional domain for future materials exploration.

Methodology

Synthesis

All preparation steps were performed in an argon atmosphere (H$_2$O < 1 ppm, O$_2$ < 1 ppm). $Li_{1+2x}Cl_{1-x}N_x$ phases: the synthesis precursors were LiCl (Sigma-Aldrich, 99%) and Li$_3$N (Sigma-Aldrich, >99.5%). Stoichiometric amounts of the precursors were milled in a planetary ball mill (Jar : ZrO$_2$, 45 mL) with 10 mm ZrO$_2$ balls and a ball : powder mass ratio of 30 at 550 rpm for 99 (5 min milling–5 min-pause) cycles. $Li_{2+x}S_{1-x}N_x$

** Even oxide garnet electrolytes may potentially benefit from protection layers against Li metal.[45,46]

3570 | *J. Mater. Chem. A*, 2025, **13**, 3562–3574

This journal is © The Royal Society of Chemistry 2025

phases (originally reported in ref. 13): the synthesis precursors were Li_2S (Sigma-Aldrich, 99%) and Li_3N (Sigma-Aldrich, >99.5%). Stoichiometric amounts of the precursors were milled in a planetary ball mill (Jar : ZrO_2, 45 mL) with 10 mm ZrO_2 balls and a ball : powder mass ratio of 30 at 550 rpm for 99 (5 min milling–5 min-pause) cycles.

Electrochemical characterization

The same procedure was applied to all solid electrolytes (SE) investigated in this work: $Li_{1+2x}Cl_{1-x}N_x$ and $Li_{2+x}S_{1-x}N_x$ and $Li_{1.9+0.55y}Cl_{0.55(1-y-z)}S_{0.55y}Br_{0.55z}N_{0.45}$. Electrochemical Impedance Spectroscopy (EIS): pellets (diameter = 10 mm) of the SE powder samples were pressed (3.2 tons) in custom-made cells. These lab cells consist of an alumina tube and two stainless steel (SS) plungers and an airtight seal. The stainless steel plungers act as current collectors. Solid electrolyte powder is filled in the alumina tube and compressed on both sides with the stainless steel plungers. The cell configuration used was SS|SE|SS. AC impedance was performed with a Metrohm Autolab (AUT86298) in the frequency range 10 MHz to 0.1 Hz with a voltage amplitude of 10 mV. EIS spectra were fitted with a resistor in parallel with a constant phase element (CPE) representing the solid electrolyte and a CPE representing the solid electrolyte–SS interface. RT conductivities were measured in ambient conditions (22 °C in our labs). Linear sweep voltammetry (LSV): LSV measurements were also performed with an Metrohm Autolab (AUT86298). To measure the anodic limit of SE phases, Li|SE|SE–C cells were used. To make the SE–C composite cathode a mixture of SE : Super P with a weight ratio of 0.7 : 0.3 was milled in a planetary ball mill (Jar : ZrO_2, 45 mL) with 10 mm ZrO_2 balls and a ball/powder ratio of 30 at 400 rpm for 2 h (5 min milling; 5 min pause). Li|SE|SE-C cells were assembled by pressing a SE pellet (130 mg, 3.2 tons) and subsequently the SE–C composite (15 mg, 3.2 tons) on top. Finally, a Li disk was placed on the opposite side of the SE pellet. The LSV scanning rate was 0.01 mV s^{-1}.

X-ray diffraction

Powder diffraction patterns were collected using Cu Kα X-rays (1.54 Å) on a PANalytical X'Pert Pro X-ray diffractometer. The air sensitive SE probes were loaded into air-tight holders in an Ar-filled glovebox prior to the measurements. GSAS-II[34] and FullProf[35] used for LeBail and Rietveld refinements. As a starting point the structure solution of Li_5NCl_2 (i.e. $Li_{1.66}Cl_{0.66}N_{0.33}$) was taken.[15] For $Li_{1+2x}Cl_{1-x}N_x$ phases with higher nitrogen content the nitrogen amount was increased, the chlorine amount reduced and the Li fraction of occupied tetrahedral sites increased according to the synthesized stoichiometry. Based on the initial structure solution of $Li_{1.66}Cl_{0.66}N_{0.33}$ [ref. 15] all Li ions were assumed in tetrahedral sites though we note that generally a small occupation of the octahedral sites (≤5%) may potentially exist (see ESI Note 1†).

Computational details

All DFT calculations were performed with the Vienna *ab initio* simulation package VASP with computational settings

consistent with those used in the Materials Project database.[36] Obtaining jump-activation energies for $Li_{1+2x}Cl_{1-x}N_x$ and LiCl. For the generation and analysis of supercells the calculations were done on 7 different $2 \times 2 \times 2$ $Li_{1+2x}Cl_{1-x}N_x$ and one $2 \times 2 \times 2$ LiCl supercells. Because of the shared site occupations and partial occupancies in $Li_{1+2x}Cl_{1-x}N_x$ phases, different atomic arrangements were generated by random decoration of the Wyckoff 4a (0, 0, 0) position with nitrogen and chlorine and the 8c (0.25, 0.25, 0.25) positions were randomly decorated with Li and vacancies. For the generation and analysis of supercells the pymatgen package was used.[37] For the AIMD simulations the Li pseudopotential was changed from one considering the semicore s electrons as valence (i.e. $1s^2 2s^1$ "Li_sv", which was used for relaxations) to on considering on the 2s electrons (i.e. $2s^1$ "Li") as this enables the use of a lower energy cutoff and vastly improves computational speed. The simulation time was 200 ps for every AIMD simulation. The AIMD simulations were executed at 1000 K. The dissection of AIMD simulations into individual jump events and subsequent analysis of jump frequencies and individual $E_{a,jump}$ values was done as first described by de Klerk and Wagemaker[18] and currently developed as a python package in our group [39]A comprehensive account can be found in ref. 18 but crucial aspects for the understanding of the reported data is presented here. Calculation of E_a, jump values between two sites: the sites are defined around the 0 K equilibrium positions of the Li ions. At every simulation step it is recorded in which site each Li ion is located or whether it is currently between two sites. From this information the jump frequency between two sites $\nu_{A\rightarrow B}$ can be calculated according to eqn (3):

$$\nu_{A\rightarrow B} = \frac{N_{A\rightarrow B}}{\tau_A} \qquad (3)$$

where $\nu_{A\rightarrow B}$ is the jump frequency for jumps from site A to site B, $N_{A\rightarrow B}$ is the number of recorded jumps from A to B, and τ_A is the time of occupation of site A. $E_{a,jump}$ is then obtained from eqn (1). This analysis can be done with the *gemdat* ref. 38 python package currently developed in our group. To obtain a picture as complete as possible for the jump processes in the disordered $Li_{1+2x}Cl_{1-x}N_x$ phases we executed the AIMD simulations on 5 supercells that together feature all of the possible site-bottleneck-site permutations in $Li_{1+2x}Cl_{1-x}N_x$ phases. A table with jump-E_a values is provided Table S7.†

Stability calculations for $Li_{1+2x}Cl_{1-x}N_x$ and for $Li_{2+x}S_{1-x}N_x$. 10 000 $2 \times 2 \times 2$ supercells were generated by randomly decorating the Wyckoff 4a (0, 0, 0) position with nitrogen and chlorine. The 8c (0.25, 0.25, 0.25) positions were also randomly decorated with Li and vacancies according to the targeted stoichiometry. Then formal charges of −3, −1, and +1 were assigned to nitrogen, chlorine and Li, respectively and the electrostatic energy ('Ewald energy') was calculated via pymatgen. Subsequently, out of the $Li_{1+2x}Cl_{1-x}N_x$ structures, 30 with the lowest Ewald energy were taken and relaxed by DFT. The energies obtained from DFT were used to calculate the energy of the hull of the $Li_{1+2x}Cl_{1-x}N_x$ phases, corrections from the materials project data base were applied and the energies for

This journal is © The Royal Society of Chemistry 2025

J. Mater. Chem. A, 2025, **13**, 3562–3574 | **3571**

the end-member phases (Li_3N and Li_2S) were also obtained from the materials project data base (see also ESI Note 4†).[36]

Data availability

Author contributions

The study was conceptualized by V. L. Simulation data were acquired by V. L. Experimental data were acquired by V. L., M. T. and Z. C. Data analysis and interpretation were done by V. L., T. F., M. T. and M. W. Writing and editing of the draft were done by V. L., T. F., M. W. The funding for this study was acquired by M. W. and T. F. The project was supervised by T. F. and M. W. All authors have approved the submitted version of the manuscript.

Conflicts of interest

There are no conflicts to declare.

Acknowledgements

References

1 T. Famprikis, P. Canepa, J. A. Dawson, M. S. Islam and C. Masquelier, Fundamentals of Inorganic Solid-State Electrolytes for Batteries, *Nat. Mater.*, 2019, **18**, 1278–1291.

2 J. Janek and W. G. Zeier, Challenges in Speeding up Solid-State Battery Development, *Nat. Energy*, 2023, **8**(3), 230–240.

3 Y. Kato, S. Hori, T. Saito, K. Suzuki, M. Hirayama, A. Mitsui, M. Yonemura, H. Iba and R. Kanno, High-Power All-Solid-State Batteries Using Sulfide Superionic Conductors, *Nat. Energy*, 2016, **1**(4), 1–7.

4 L. Zhou, A. Assoud, Q. Zhang, X. Wu and L. F. Nazar, New Family of Argyrodite Thioantimonate Lithium Superionic Conductors, *J. Am. Chem. Soc.*, 2019, **141**(48), 19002–19013.

5 M. A. Kraft, S. Ohno, T. Zinkevich, R. Koerver, S. P. Culver, T. Fuchs, A. Senyshyn, S. Indris, B. J. Morgan and W. G. Zeier, Inducing High Ionic Conductivity in the Lithium Superionic Argyrodites $Li_{6+x}P_{1-x}Ge_xS_5I$ for All-Solid-State Batteries, *J. Am. Chem. Soc.*, 2018, **140**(47), 16330–16339.

6 N. Kamaya, K. Homma, Y. Yamakawa, M. Hirayama, R. Kanno, M. Yonemura, T. Kamiyama, Y. Kato, S. Hama and K. A. Kawamoto, Lithium Superionic Conductor, *Nat. Mater.*, 2011, **10**(9), 682–686.

7 Y. Zhu, X. He and Y. Mo, First Principles Study on Electrochemical and Chemical Stability of Solid Electrolyte-Electrode Interfaces in All-Solid-State Li-Ion Batteries, *J. Mater. Chem. A*, 2016, **4**(9), 3253–3266.

8 H. Huo and J. Janek, Silicon as Emerging Anode in Solid-State Batteries, *ACS Energy Lett.*, 2022, **7**(11), 4005–4016.

9 W. Zaman and K. B. Hatzell, Processing and Manufacturing of next Generation Lithium-Based All Solid-State Batteries, *Curr. Opin. Solid State Mater. Sci.*, 2022, **26**(4), 101003.

10 V. Landgraf, T. Famprikis, J. de Leeuw, L. J. Bannenberg, S. Ganapathy and M. Wagemaker, Li_5NCl_2: A Fully-Reduced, Highly-Disordered Nitride-Halide Electrolyte for Solid-State Batteries with Lithium-Metal Anodes, *ACS Appl. Energy Mater.*, 2023, **6**(3), 1661–1672.

11 C. Szczuka, B. Karasulu, M. F. Groh, F. N. Sayed, T. J. Sherman, J. D. Bocarsly, S. Vema, S. Menkin, S. P. Emge, A. J. Morris and C. P. Grey, Forced Disorder in the Solid Solution $Li_3P–Li_2S$: A New Class of Fully Reduced Solid Electrolytes for Lithium Metal Anodes, *J. Am. Chem. Soc.*, 2022, **144**(36), 16350–16365.

12 X. Xu, G. Du, C. Cui, J. Liang, C. Zeng, S. Wang, Y. Ma and H. Li, Stabilizing the Halide Solid Electrolyte to Lithium by a β-Li_3N Interfacial Layer, *ACS Appl. Mater. Interfaces*, 2022, **14**(35), 39951–39958.

13 V. Landgraf, M. Tu, Z. Cheng, J. de Leeuw, S. Ganapathy, M. Wagemaker and T. Famprikis, Entropy-Induced High Conductivity in Fully-Reduced Electrolytes for Solid-State Batteries with Lithium Metal Anodes, *ChemRxiv*, 2023, preprint, DOI: 10.26434/chemrxiv-2023-33r87.

14 W. Li, M. Li, P.-H. Chien, S. Wang, C. Yu, G. King, Y. Hu, Q. Xiao, M. Shakouri and R. Feng, Lithium-Compatible and Air-Stable Vacancy-Rich $Li_9N_2Cl_3$ for High–Areal Capacity, Long-Cycling All–Solid-State Lithium Metal Batteries, *Sci. Adv.*, 2023, **9**(42), eadh4626.

15 R. Marx and H. M. Mayer, Preparation and Crystal Structure of Ordered and Disordered Lithium Nitride Dichloride, Li_5NCl_2, *J. Solid State Chem.*, 1997, **130**(1), 90–96.

16 W. Weppner, P. Hartwig and A. Rabenau, Consideration of Lithium Nitride Halides as Solid Electrolytes in Practical Galvanic Cell Applications, *J. Power Sources*, 1981, **6**(3), 251–259.

17 R. D. Shannon, Revised Effective Ionic Radii and Systematic Studies of Interatomic Distances in Halides and

3572 | *J. Mater. Chem. A*, 2025, **13**, 3562–3574

This journal is © The Royal Society of Chemistry 2025
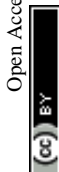
Chalcogenides, *Acta Crystallogr., Sect. A*, 1976, **32**(5), 751–767.

18 N. J. J. De Klerk, E. Van Der Maas and M. Wagemaker, Analysis of Diffusion in Solid-State Electrolytes through MD Simulations, Improvement of the Li-Ion Conductivity in β-Li$_3$PS$_4$ as an Example, *ACS Appl. Energy Mater.*, 2018, **1**(7), 3230–3242.

19 C. Yu, S. Ganapathy, N. J. J. De Klerk, I. Roslon, E. R. H. Van Eck, A. P. M. Kentgens and M. Wagemaker, Unravelling Li-Ion Transport from Picoseconds to Seconds: Bulk versus Interfaces in an Argyrodite Li$_6$PS$_5$Cl-Li$_2$S All-Solid-State Li-Ion Battery, *J. Am. Chem. Soc.*, 2016, **138**(35), 11192–11201.

20 N. J. J. De Klerk, I. Rosłoń and M. Wagemaker, Diffusion Mechanism of Li Argyrodite Solid Electrolytes for Li-Ion Batteries and Prediction of Optimized Halogen Doping: The Effect of Li Vacancies, Halogens, and Halogen Disorder, *Chem. Mater.*, 2016, **28**(21), 7955–7963.

21 N. J. J. De Klerk and M. Wagemaker, Diffusion Mechanism of the Sodium-Ion Solid Electrolyte Na$_3$PS$_4$ and Potential Improvements of Halogen Doping, *Chem. Mater.*, 2016, **28**(9), 3122–3130.

22 X. Li, H. Liu, C. Zhao, J. T. Kim, J. Fu, X. Hao, W. Li, R. Li, N. Chen, D. Cao, Z. Wu, Y. Su, J. Liang and X. Sun, Hopping Rate and Migration Entropy as the Origin of Superionic Conduction within Solid-State Electrolytes, *J. Am. Chem. Soc.*, 2023, **145**(21), 11701–11709.

23 N. Flores-González, N. Minafra, G. Dewald, H. Reardon, R. I. Smith, S. Adams, W. G. Zeier and D. H. Gregory, Mechanochemical Synthesis and Structure of Lithium Tetrahaloaluminates, LiAlX$_4$(X = Cl, Br, I): A Family of Li-Ion Conducting Ternary Halides, *ACS Mater. Lett.*, 2021, **3**(5), 652–657.

24 J. Janek and W. G. Zeier, A Solid Future for Battery Development, *Nat. Energy*, 2016, **1**(9), 1–4.

25 Y. Zhu, X. He and Y. Mo, Origin of Outstanding Stability in the Lithium Solid Electrolyte Materials: Insights from Thermodynamic Analyses Based on First-Principles Calculations, *ACS Appl. Mater. Interfaces*, 2015, **7**(42), 23685–23693.

26 T. K. Schwietert, V. A. Arszelewska, C. Wang, C. Yu, A. Vasileiadis, N. J. J. de Klerk, J. Hageman, T. Hupfer, I. Kerkamm and Y. Xu, Clarifying the Relationship between Redox Activity and Electrochemical Stability in Solid Electrolytes, *Nat. Mater.*, 2020, **19**(4), 428–435.

27 S. Wang, Q. Bai, A. M. Nolan, Y. Liu, S. Gong, Q. Sun and Y. Mo, Lithium Chlorides and Bromides as Promising Solid-State Chemistries for Fast Ion Conductors with Good Electrochemical Stability, *Angew. Chem., Int. Ed.*, 2019, **58**(24), 8039–8043.

28 K. Subramanian, G. V. Alexander, K. Karthik, S. Patra, M. S. Indu, O. V. Sreejith, R. Viswanathan, J. Narayanasamy and R. Murugan, A Brief Review of Recent Advances in Garnet Structured Solid Electrolyte Based Lithium Metal Batteries, *J. Energy Storage*, 2021, **33**, 102157.

29 L. M. Riegger, R. Schlem, J. Sann, W. G. Zeier and J. Janek, Lithium-Metal Anode Instability of the Superionic Halide

30 Solid Electrolytes and the Implications for Solid-State Batteries, *Angew. Chem.*, 2021, **133**(12), 6792–6797.

30 M. Du, K. Liao, Q. Lu and Z. Shao, Recent Advances in the Interface Engineering of Solid-State Li-Ion Batteries with Artificial Buffer Layers: Challenges, Materials, Construction, and Characterization, *Energy Environ. Sci.*, 2019, **12**(6), 1780–1804.

31 P. Yu, H. Zhang, F. Hussain, J. Luo, W. Tang, J. Lei, L. Gao, D. Butenko, C. Wang, J. Zhu, W. Yin, H. Zhang, S. Han, R. Zou, W. Chen, Y. Zhao, W. Xia and X. Sun, Lithium Metal-Compatible Antifluorite Electrolytes for Solid-State Batteries, *J. Am. Chem. Soc.*, 2024, **146**(18), 12681–12690.

32 T. Krauskopf, F. H. Richter, W. G. Zeier and J. Janek, Physicochemical Concepts of the Lithium Metal Anode in Solid-State Batteries, *Chem. Rev.*, 2020, **120**(15), 7745–7794.

33 K. B. Hatzell, X. C. Chen, C. L. Cobb, N. P. Dasgupta, M. B. Dixit, L. E. Marbella, M. T. Mcdowell, P. P. Mukherjee, A. Verma, V. Viswanathan, A. S. Westover and W. G. Zeier, Challenges in Lithium Metal Anodes for Solid-State Batteries, *ACS Energy Lett.*, 2020, **5**(3), 922–934.

34 B. H. Toby and R. B. Von Dreele, GSAS-II: The Genesis of a Modern Open-Source All Purpose Crystallography Software Package, *J. Appl. Crystallogr.*, 2013, **46**(2), 544–549.

35 J. Rodriguez-Carvajal, Recent advances in magnetic structure determination by neutron powder diffraction, *Phys. B*, 1993, **192**, 55, DOI: 10.1016/0921-4526(93)90108-I.

36 A. Jain, S. P. Ong, G. Hautier, W. Chen, W. D. Richards, S. Dacek, S. Cholia, D. Gunter, D. Skinner, G. Ceder and K. A. Persson, Commentary: The Materials Project: A Materials Genome Approach to Accelerating Materials Innovation, *APL Mater.*, 2013, **1**(1), 001002.

37 S. P. Ong, W. D. Richards, A. Jain, G. Hautier, M. Kocher, S. Cholia, D. Gunter, V. L. Chevrier, K. A. Persson and G. Ceder, Python Materials Genomics (Pymatgen): A Robust, Open-Source Python Library for Materials Analysis, *Comput. Mater. Sci.*, 2013, **68**, 314–319.

38 V. Azizi; S. Smeets; A. K. Lavrinenko; S. Ciarella and T. Famprikis, GEMDAT, Zenodo, July 2024.

39 C. R. Harris, K. J. Millman, S. J. Van Der Walt, R. Gommers, P. Virtanen, D. Cournapeau, E. Wieser, J. Taylor, S. Berg and N. J. Smith, Array Programming with NumPy, *Nature*, 2020, **585**(7825), 357–362.

40 J. D. Hunter, Matplotlib: A 2D Graphics Environment, *Comput. Sci. Eng.*, 2007, **9**(3), 90–95.

41 C. R. A. Catlow, Static Lattice Simulation of Structure and Transport in Superionic Conductors, *Solid State Ionics*, 1983, **8**(SUPPL. 3), 89–107.

42 R. Marx, F. Lissner and T. Schleid, Li$_9$N$_2$S$_3$: Das Erste Nitridsulfid Der Alkalimetalle in Einer Li2O-Typ-Variante, *Z. Anorg. Allg. Chem.*, 2006, **632**(12-13), 2151.

43 Z. Deng, T. P. Mishra, E. Mahayoni, Q. Ma, A. J. K. Tieu, O. Guillon, J.-N. Chotard, V. Seznec, A. K. Cheetham and C. Masquelier, Fundamental Investigations on the Sodium-Ion Transport Properties of Mixed Polyanion Solid-State Battery Electrolytes, *Nat. Commun.*, 2022, **13**(1), 4470.

44 M. Wilkening, D. Gebauer and P. Heitjans, Diffusion Parameters in Single-Crystalline L$_{i3}$N as Probed by ^{6}Li and

This journal is © The Royal Society of Chemistry 2025

J. Mater. Chem. A, 2025, **13**, 3562–3574 | **3573**

^{7}Li Spin-Alignment Echo NMR Spectroscopy in Comparison with Results from [8]Li β-Radiation Detected NMR, *J. Phys. Condens. Matter*, 2007, **20**(2), 22201.

45 H. Xu, Y. Li, A. Zhou, N. Wu, S. Xin, Z. Li and J. B. Goodenough, Li_3N-Modified Garnet Electrolyte for All-Solid-State Lithium Metal Batteries Operated at 40 °C, *Nano Lett.*, 2018, **18**(11), 7414–7418.

46 C. Zhu, T. Fuchs, S. A. L. Weber, F. H. Richter, G. Glasser, F. Weber, H. J. Butt, J. Janek and R. Berger, Understanding the Evolution of Lithium Dendrites at $Li_{6.25}Al_{0.25}La_3Zr_2O_{12}$ Grain Boundaries via Operando Microscopy Techniques, *Nat. Commun.*, 2023, **14**(1), 1300.

3574 | *J. Mater. Chem. A*, 2025, **13**, 3562–3574

This journal is © The Royal Society of Chemistry 2025